EDGE ARTICLE

Check for updates

Addressing the autofluorescence issue in deep tissue imaging by two-photon microscopy: the significance of far-red emitting dyes†

Yong Woong Jun, [ID] ‡ Hye Rim Kim,‡ Ye Jin Reo, [ID] Mingchong Dai and Kyo Han Ahn [ID] *

The fluorescence imaging of tissue is essential for studying biological events beyond the cellular level. Two-photon microscopy based on the nonlinear light absorption of fluorescent dyes is a viable tool for the high resolution imaging of tissue. A key limitation for deep tissue imaging is the autofluorescence from intrinsic biomolecules. Here, we report a systematic study that discloses relative autofluorescence interference, which is dependent on the type of tissue and the excitation and emission wavelengths in two-photon imaging. Among the brain, kidney, liver, lung, and spleen mouse tissues examined, the kidney tissue exhibited prominent autofluorescence followed by the liver and others. Notably, regardless of the tissue type, prominent autofluorescence is observed not only from the green emission channel but also from the yellow emission channel where common two-photon absorbing dyes also emit, whereas there is minimal autofluorescence from the red channel. The autofluorescence is slightly influenced by the excitation wavelength. Toward minimal autofluorescence, we developed a new class of two-photon absorbing dyes that are far-red emitting, water-soluble, and very bright inside cells as well as in tissue. A comparative assessment of the imaging depth, which is dependent on the three selected dyes that emit in the blue-green, yellow, and far-red regions, shows the importance of far-red emitting dyes for deep tissue imaging.

Introduction

The fluorescence imaging of tissue by two-photon microscopy (2PM) has gained increasing importance in studying biological processes beyond the cellular level. A tumor tissue specimen of one cubic centimeter, for example, consists of approximately one billion cells.[1] Accordingly, the fluorescence imaging of tissue offers "collective" information on the cellular processes, representing a more tangible biological status of living species. Acquisition of high resolution images of tissue at increasing depths by conventional one-photon confocal laser scanning microscopy (CLSM), however, presents a major challenge, limiting tissue imaging to only a shallow depth, after which the scattering of light becomes a serious issue. On the other hand, 2PM based on the two-photon (2P) excitation process with pulsed laser light enables focal-point excitation, exciting only a tiny volume (~femtolitre) around the focal point, which alleviates the scattering issues and provides high resolution images.[2,3] This nonlinear excitation process using an excitation wavelength that is double that of the one used in one-photon microscopy (1PM) offers other advantages for tissue imaging by 2PM, such as reduced photodamage and photobleaching, in addition to the increased imaging depth. Currently, we can image tissue typically down to several hundred micrometers (500 μm or so) using 2PM.[4] Therefore, 2PM has become an essential tool for long term, live cell/tissue imaging as well as for deep tissue imaging with subcellular resolution. Examples include the *in vivo* imaging of blood flow, neuronal activity in the cortex of rodent brains, the flow of retinoids in relation to tissue architecture, and biochemical reactions in living eyes.[5–8] In the last two decades since 2PM was introduced by Denk and Webb,[2,3] significant effort has been made to further increase the imaging depth by improving instrumentation.[4,9–11] Along with this research, which has led to an imaging depth of one millimeter or so, more studies have been also carried out to develop 2P absorbing dyes with higher efficiency.[12–14] As a result, 2P absorbing dyes with large two-photon absorption cross-section (TPACS) values, for example over 1000 GM, are currently available.[12,15] However, these dyes are large in size and highly hydrophobic, causing them to be sparingly soluble in aqueous media and thus this limits their use in the 2P imaging of biological systems. A handful of dyes with molecular weights of several hundred, such as acedan (2-acetyl-6-aminonaphthalene), naphthalimide, and rhodamine dyes, are

Department of Chemistry, Pohang University of Science and Technology (POSTECH), 77 Cheongam-Ro, Nam-Gu, Pohang, Gyeongbuk, Republic of Korea 37673. E-mail: ahn@postech.ac.kr

† Electronic supplementary information (ESI) available: Materials and procedures regarding the synthesis of all of the dyes, photophysical properties and tissue and cell imaging. See DOI: 10.1039/c7sc03362a

‡ These authors contributed equally.

currently used in tissue imaging[16] but these dyes cause significant autofluorescence (see below).

As the imaging of tissue with the aid of 2P dyes is receiving ever increasing attention in biomedical science, it is necessary to comprehend the fundamental issues that are associated with deep tissue imaging. A critical issue that limits the imaging depth is autofluorescence from intrinsic biomolecules such as nicotinamide adenine dinucleotide (NADH and its phosphate analogue NADPH), riboflavin, flavoproteins, aromatic amino acids, *etc.* These biomolecules have low TPACS values[17] but can cause significant autofluorescence in tissue imaging. Their distribution and relative percentages in biological organs can be different, which would expose different levels of autofluorescence depending on the type of organ tissue. As these biomolecules have different absorption and emission wavelengths, the magnitude of autofluorescence should also be dependent on both the absorption and emission wavelengths of the dye used. Under 2P imaging conditions, we can minimize the absorption from these biomolecules by exciting at near-infrared (NIR) excitation wavelengths, leaving the emission wavelength of the dye as a remaining issue (see below). Therefore, the development of 2P absorbing dyes that emit in the far-red region and have sufficient water solubility, photostability, and high cellular brightness is of great importance for bioimaging applications. However, currently available fluorophores that satisfy the criteria are rare (Table S5 in the ESI†).[18]

In spite of the current widespread usage of 2PM in the scientific community, information on the autofluorescence that is dependent on the tissue as well as the excitation and emission wavelengths is rather sporadic or unavailable. Therefore, a systematic study on tissue and wavelength dependent autofluorescence would provide a basic guideline for deep tissue imaging and also for our attempts to develop 2P absorbing dyes and probes that are desirable for deep tissue imaging. In this contribution, we reveal that the autofluorescence is indeed highly dependent on the tissue type as well as the excitation and emission wavelengths. Notably, we have found that significant autofluorescence comes from the emission collected not only in the green but also in the yellow wavelength regions. In contrast, autofluorescence from the red region is minimal. Consequently, autofluorescence should be seriously taken into account when we conduct tissue imaging using the common 2P absorbing dyes and the corresponding fluorescent probes that mostly emit in the green and yellow wavelength regions. On the other hand, the use of far-red/NIR emitting 2P absorbing dyes is highly recommended to minimize autofluorescence interference from the intrinsic biomolecules and hence to increase the tissue imaging depth. The latter result prompts us to develop a novel class of 2P absorbing dyes that emit in the far-red or NIR region and have other promising properties for bioimaging applications.

Results and discussion

Autofluorescence in tissue imaging

Under 2P excitation in the near-infrared (NIR) wavelength region (750–1000 nm), we may expect insignificant absorption and hence minimal emission from the endogenous biomolecules. However, this is not the case in reality. Biomolecules such as NADH, folic acid, and retinol have emission maxima in the range of 450–500 nm, and riboflavin, flavin coenzymes, and flavoproteins have emission maxima in the range of 520–540 nm. Among them, NAD(P)H and riboflavin (and its protein conjugates flavoproteins) are mostly responsible for the autofluorescence interference in the blue-green and green-yellow emission regions, respectively.[19] Even though these biomolecules have small two-photon action cross-section values ($\Phi_F\sigma_2 \le$ 1 GM),[17] their cellular concentrations are rather high (for example, ~107 FAD molecules per cell (ref. 20)) and hence may cause significant autofluorescence interference in tissue imaging. Indeed, fluorescence from these biomolecules has been explored when studying their biological roles without the aid of an external dye or probe.[21] The emission wavelengths of commonly used 2P dyes, which are typically in the visible region below 625 nm can have significant overlap with the emission bands from the intrinsic biomolecules.

In this study, we have assessed intrinsic autofluorescence in tissue imaging which is dependent on three variables: the type of organ tissue, the 2P excitation wavelength, and the emission window. First, the autofluorescence intensity was compared amongst different mouse organ tissues (brain, kidney, liver, lung, and spleen) by exciting at different wavelengths (800, 850, and 900 nm) and collecting the fluorescence through different optical windows (blue, green, yellow, and red channels). Next, the effect of autofluorescence on the imaging depth, which is dependent on the emission windows, was evaluated using three selected TP dyes; the dyes have a comparable level of two-photon brightness ($\Phi_F\sigma_2$) but emit at different wavelengths from blue to red, letting us assume that the brightness of the dyes barely affects the imaging depth in these experiments. To this end, we have developed a novel class of 2P absorbing dyes that emit in the far-red region.

To analyze autofluorescence in tissue imaging systematically, we set up a 2P microscope as described in Fig. 1a. Four different emission filter sets were used to collect fluorescence in the wavelength regions of 430–480 nm (blue channel), 500–550 nm (green channel), 565–605 nm (yellow channel), and 625–675 nm (red channel), separately. Three laser sources, 800 nm, 850 nm, and 900 nm, were applied to excite biomolecules in the tissue because most of the small-molecular 2P dyes have maximum 2P absorbance in the range of 800–900 nm, which also falls in the first biological optical window where interference from biomolecules and water is minimal.[22]

In this experimental set-up, we aimed to figure out: (1) to what extent autofluorescence between different organ tissues varies, (2) which excitation wavelength causes the least autofluorescence, and (3) which emission window offers the least interference from autofluorescence (Fig. 1).

Tissue samples were prepared by removing the brain, lung, liver, spleen, and kidney organs from a mouse, followed by sectioning to an approximate size of 400 μm × 400 μm × 50 μm. Each of the tissue sections were imaged in the four channels at every 2 μm depth from the surface to the inside layer, and further down to the bottom (50 μm depth), under excitation at
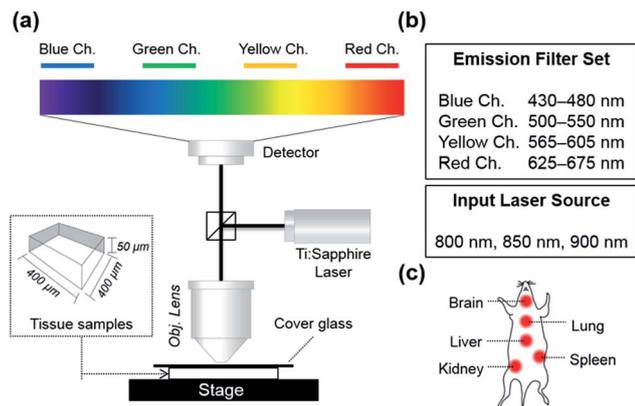
Fig. 1 (a) The experimental set-up for mouse tissue imaging by 2PM. (b) The wavelength ranges of selected emission filter sets and input laser sources. (c) Five mouse organs used for the preparation of the tissue samples.

each of the given wavelengths (Fig. 2a). Fig. 2b shows the cross-section images at a depth of 14 μm depending on the excitation and emission wavelengths. It is notable that, in these cross-section images, strong autofluorescence is observed, particularly from the yellow channel in addition to the green channel, whereas minimal autofluorescence is observed from the red channel. An average autofluorescence value was calculated from a total of 25 images obtained at every 2 μm of depth for a given tissue at different emission channels and excitation wavelengths. Among the organs, the kidney shows the strongest autofluorescence, with ∼5 times higher intensity with respect to that of the brain, followed by the liver (∼2.5 times), lung (∼1.3 times), and spleen (∼1.1 times). Notably, in all of the five organs autofluorescence from the red channel is minimal and much lower than that from the other channels (Fig. 2c). In comparison, in both cases of kidney and liver, the autofluorescence from the red channel is only about 15% of that from the yellow channel. The autofluorescence is also affected by the excitation wavelength, albeit a little, showing lower autofluorescence when excited at 900 nm compared to at 850 or at 800 nm (Fig. 2d). This is plausibly due to the minimal two-photon absorption by the key biomolecules when they are excited around 900 nm.[18] Through autofluorescence analysis, it is concluded that autofluorescence interference is minimal when the images are obtained under excitation at around 900 nm and, above all, when emission is collected from the red emission channel.

Additionally, this study warns us to take possible autofluorescence interference into account when interpreting the imaging data obtained with the common 2P dyes that emit in the green or yellow region (λ_{em} = 500–625 nm). All together there is a huge demand for fluorophores that emit in the far-red (λ_{em} = 650–700 nm) or NIR region, in addition to having desirable 2P absorption efficiency near 900 nm, good photostability, high cellular brightness, proper solubility in aqueous media, and biocompatibility.

Far-red emitting, two-photon absorbing dyes

Given the minimal autofluorescence results from the red emission channel in the tissue imaging, we set out to develop 2P absorbing dyes that emit in the far-red region. For bioimaging applications, the water solubility of the dyes is another critical property that is required, in addition to other factors such as having good brightness, photostability, synthetic feasibility, and biocompatibility.

7-Amino-coumarin dyes, which have good photostability and intramolecular charge transfer (ICT) character, may offer a good starting point to develop 2P absorbing, far-red emitting dyes through elongation of the π-conjugation.[23–26] In this work, we have investigated such a π-extended coumarin system, that is, benzocoumarin derivatives with a pyridinium substituent.

The pyridinium group is expected to act as a strong electron-acceptor as well as to increase the water solubility of the dyes (Fig. 3a). A structurally related benzocoumarin, IminoPOS, which was previously developed by us, emits in the orange region (λ_{abs} = 446 nm, λ_{em} = 585 nm; in EtOH).[27] A pyridyl-benzocoumarin that has a dimethylamino donor (**PyBC580a**) and its derivatives can be readily synthesized in high yields by esterification followed by *in situ* Knoevenagel condensation between 2-hydroxy-7-(di- or mono-alkylamino) naphthalene-3-aldehyde (**1**) and 4-pyridylacetic acid (Scheme 1).[28] **PyBC580a** also emits in the orange region, at around 585 nm. Gratifyingly, its salt, a pyridinium-benzocoumarin **Py⁺BC680a** emits in the desired far-red region even in ethanol (λ_{abs} = 512 nm, λ_{em} = 680 nm) (Fig. 3c and d).

The HOMO–LUMO energy levels computed for these compounds show a progressive decrease in the energy gaps upon increasing the π-conjugation and ICT character (Fig. 3b). Therefore, by increasing the π-conjugation and ICT character, a huge bathochromic shift (234 nm) is achieved. Above all, the introduction of the pyridinium group provides the new dyes with high water solubility (>100 μM, Fig. S3, ESI†). By changing the amine donor to pyrrolidine, a further bathochromic shift can be attained,[29,30] as seen by **Py⁺BC690** (λ_{abs} = 527 nm, λ_{em} = 691 nm, in EtOH). The pyridinium-benzocoumarins have a good level of 2P brightness ($\Phi_F\sigma_2$ = 160 and 150 GM for **Py⁺BC690** and **Py⁺BC680b**, respectively; Fig. S5, ESI†) and also show bright cellular images (Fig. S4, ESI†), although their fluorescence quantum yields (Φ_F = 5–8%) are marginal, which is similar other dyes that are far-red emitting and water-soluble.[31] The zwitterionic, charge neutral analogue **Py⁺O⁻BC600** shows a much higher fluorescence quantum yield (Φ_F = 49%). This contrasting result suggests that the low quantum efficiency of the ionic dyes may be ascribed to solvent-assisted non-radiative decay.[32] The photophysical properties of the new dyes are summarized in Table 1. The **Py⁺BC** dyes thus constitute a novel class of 2P absorbing dyes that emit in the far-red wavelength region, which have various additional promising properties for bioimaging applications: they are highly soluble in water, readily synthesized and derivatized, small in size, photostable (Fig. S9 and S10, ESI†), cell- and tissue-permeable, and biocompatible. Above all, they show bright fluorescent images inside cells, as well as in tissue (see below
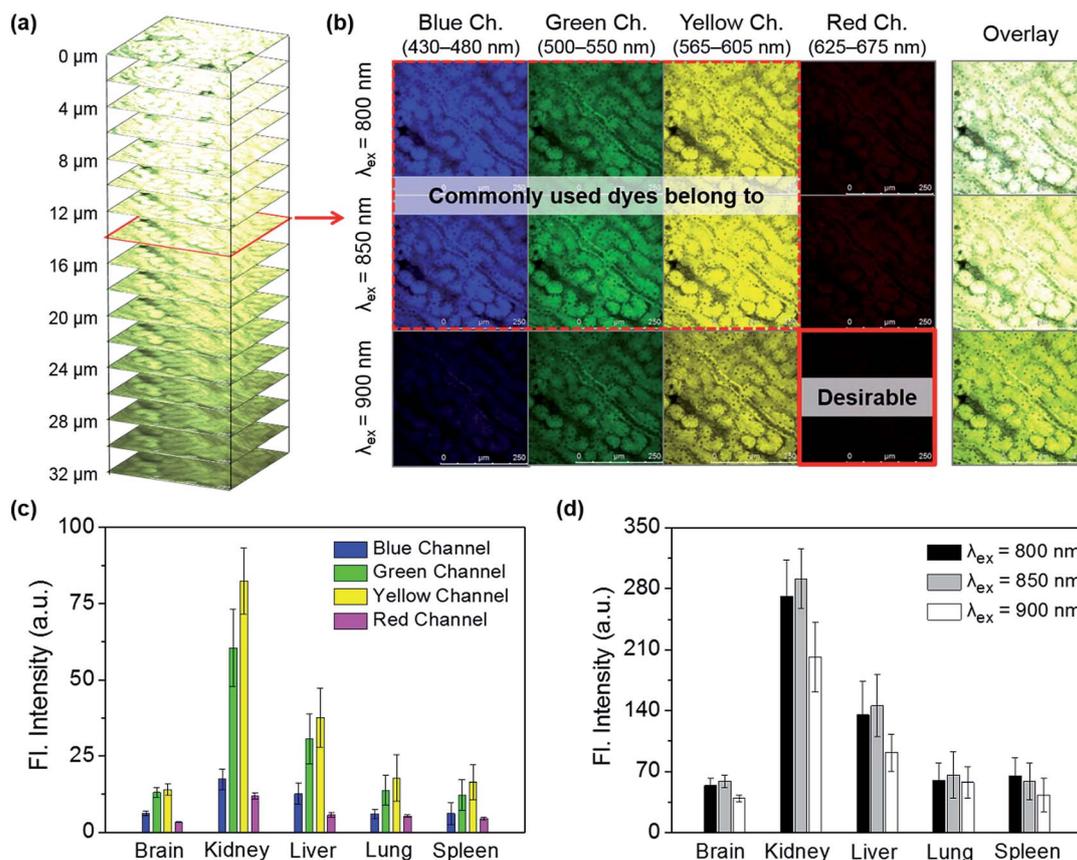
Fig. 2 (a) Autofluorescence images of a kidney tissue sample, z-stacked from the surface to 32 μm depth and obtained under excitation at 850 nm. (b) Autofluorescence images of the kidney tissue at a depth of 14 μm, obtained by exciting at different excitation wavelengths (800, 850, and 900 nm) and collecting through different emission channels (blue, 430–480 nm; green, 500–550 nm; yellow, 565–605 nm; red, 625–675 nm). (c) Comparison of the total autofluorescence intensity, which is dependent on the organ tissues (brain, kidney, liver, lung, and spleen) and the emission channels; each bar graph represents the total fluorescence intensity of all of the z-stacked images (shown in "(a)") that were obtained by exciting at 850 nm and collecting through the given emission channel. (d) Comparison of the total autofluorescence intensity, which is dependent on the organ tissues and excitation wavelengths (800, 850, and 900 nm); each bar graph represents the total fluorescence intensity of all of the z-stacked images (shown in "(a)") that were obtained by exciting at the given wavelength and collecting through the whole channel. The laser power was 95 mW at the focal point. The scale bar is 250 μm.

and Fig. S4 and S8, ESI†). It should be noted that a bright dye in cellular imaging does not guarantee bright tissue imaging. To our knowledge, the existing 2P dyes barely meet all of these criteria.

Dye-dependent tissue imaging depth

To verify the importance of a far-red emitting dye in deep tissue imaging and also to figure out the imaging depth, which is dependent on the emission wavelength of a dye, 2P imaging of kidney tissue has been conducted with three selected dyes: acedan, IminoPOS, and the newly invented **Py⁺BC690**. These fluorophores emit in different channels but have a comparable level of 2P brightness; acedan emits in the blue and green channel ($\Phi_F\sigma_2 = 80$ GM; excitation at 800 nm), IminoPOS emits in the yellow channel ($\Phi_F\sigma_2 = 84$ GM; excitation at 850 nm), and **Py⁺BC690** emits in the red channel ($\Phi_F\sigma_2 = 56$ GM; excitation at 900 nm) (Fig. 4a).

Therefore, we assume that the effect of the two-photon brightness of the dyes on the imaging depth is not significant

in comparison to that of the emission wavelength. Kidney tissue was chosen for the comparison study because it exhibits the strongest autofluorescence among the examined tissues: the kidney contains abundant blood which absorbs and scatters light, so that it makes the deep tissue imaging of kidney challenging.[33] Dissected kidney tissue samples were incubated with each of the fluorophores (10 μM in pH 7.4 HEPES buffer) for 24 h. Each tissue sample was then imaged using 2PM (Fig. 1) from the surface to inside tissue. The results are summarized in Fig. 4. Near the surface region (down to 50 μm or so), all of the fluorophores afford images with sufficient signal-to-noise (S/N) ratios of higher than three, disclosing distinct morphology (Fig. 4b). It is thus concluded that such blue-green, yellow, and far-red emitting dyes having a good level of 2P brightness and can be used to image tissue near the surface region with negligible autofluorescence interference. In all of the cases, bright and distinct tissue images are observed at 25 μm (Fig. 4b). When it comes to the imaging of tissue below the surface layer (>50 μm) and down to a mid-depth (~150 μm), the

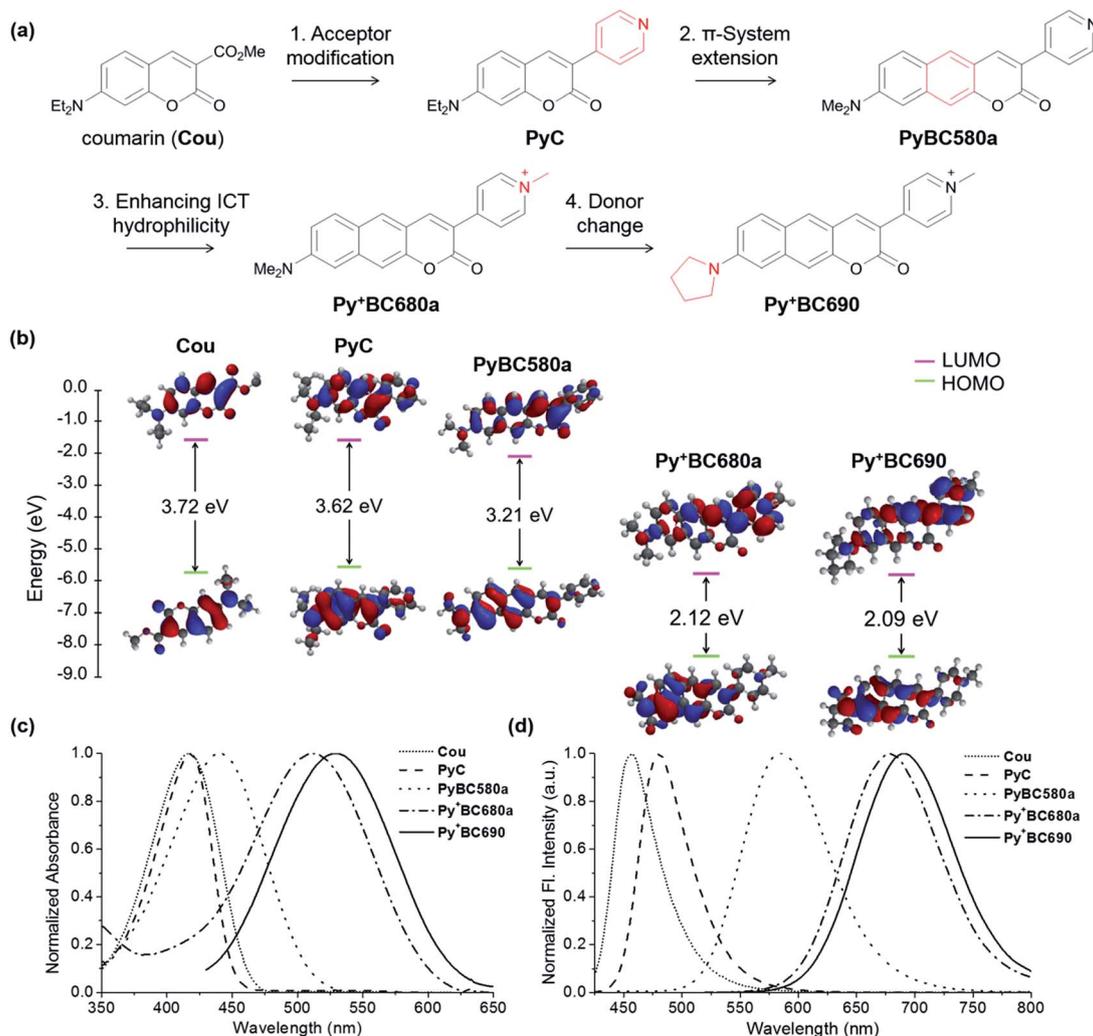Fig. 3 (a) The systematic structure variation toward the **Py⁺BC** dyes **680a** and **690**. (b) The HOMO−LUMO of a coumarin, **PyC**, **PyBC580a**, and **Py⁺BC** dyes and their relative energies, calculated using the density function of B3LYP/6-31G*. The normalized (c) absorption and (d) emission spectra of the dyes at 10 μM in EtOH.

S/N ratio begins to deviate depending on the dyes; the blue-green and yellow emitting dyes barely meet the criterion of a S/N ratio of three that is necessary to distinguish the signal from the noise level, whereas the far-red emitting dye still possesses higher S/N ratio values. An even worse situation is observed beneath an imaging depth of ∼150 μm; after this point, the S/N ratio becomes smaller than three for both of the blue-green and yellow emitting dyes, meaning that they do not offer images that show discernable morphology any more. In contrast, the far-red emitting dye still has a S/N ratio of higher than three even down to 210 μm and provides images that show discernable morphology.
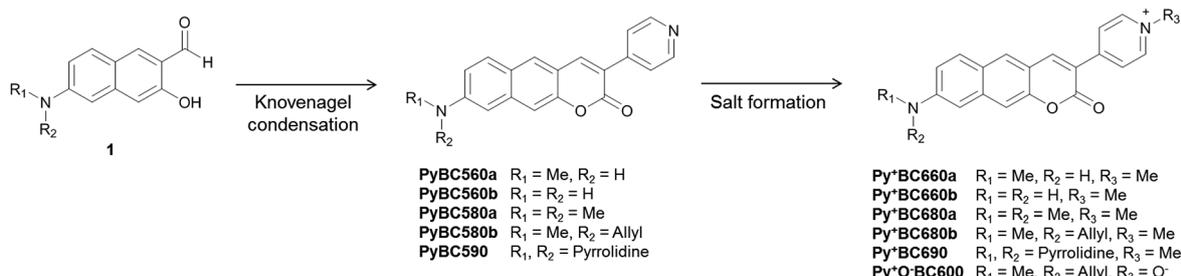
Scheme 1 Synthesis of **Py⁺BC** derivatives.

Table 1 The photophysical properties of the Py$^+$BC dyes[a]

Compounds	λ_{abs} (nm)	ε[b]	λ_{em}[c] (nm)	Φ_F[d]	Φ_F[e]	Φ_F[f]	Brightness[d] ($\varepsilon \times \Phi_F$)	$\Phi_F\sigma_2$[g] (GM)
Py$^+$BC690	527	27 577	691	0.029	0.048	0.037	799	160
Py$^+$BC680a	513	34 818	681	0.060	0.070	0.082	2089	n.d.[h]
Py$^+$BC680b	511	17 258	680	0.068	0.063	0.072	1173	150
Py$^+$BC660a	506	12 915	663	0.058	0.070	0.073	749	n.d.[h]
Py$^+$BC660b	499	11 593	660	0.044	0.063	0.054	510	n.d.[h]
Py$^+$O$^-$BC600	456	35 464	606	0.097	0.398	0.489	3440	n.d.[h]

[a] All of the measurements were conducted at 25 °C with the compounds (10 μM) dissolved in ethanol. [b] L mol^{-1} cm^{-1}. [c] Measured under excitation at the maximum absorption wavelength of the dyes in EtOH. [d] Fluorescence quantum yields determined in EtOH using rhodamine 6G as a reference dye (Φ_F = 0.91 in EtOH). [e] Fluorescence quantum yields determined in CH$_3$CN using rhodamine 6G as a reference dye (Φ_F = 0.91 in EtOH). [f] Fluorescence quantum yields determined in CH$_2$Cl$_2$ using rhodamine 6G as a reference dye (Φ_F = 0.91 in EtOH). [g] All of the measurements were conducted with the compounds (100 μM) dissolved in DMSO. Rhodamine B was used as a reference. [h] n.d. = not determined.

Brain tissue imaging

Finally, one of the far-red emitting dyes, **Py$^+$BC690**, that showed the lowest autofluorescence interference among the five tissues that were examined was applied to the imaging of brain tissue. We can clearly see the deep tissue area after an optical clearing process (BABB-clearing)[34] at this stage down to 1380 μm, which is the maximum working distance of the lens that we have

(Fig. 5 and S8, ESI†). The clear images in the deep tissue area from any direction (Fig. 5a–c) also suggest the high tissue-penetration ability of the dye, which is also an important feature. It is thus expected that far-red or NIR emitting dyes with higher 2P brightness will enable us to look into tissue even farther with sufficient resolution.
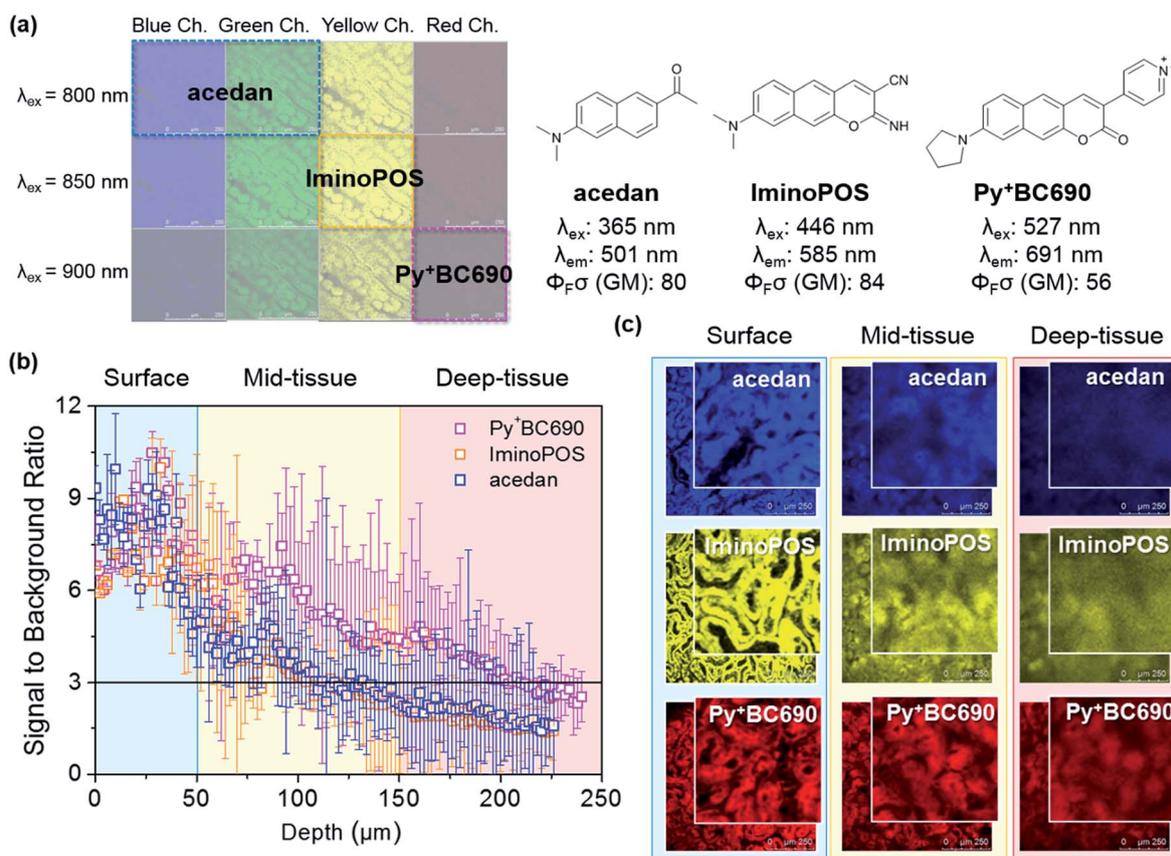

Fig. 4 (a) A diagram representing the excitation and emission wavelengths of the selected dyes (acedan, IminoPOS, and **Py$^+$BC690**) and their key optical properties. (b) A collected presentation of S/N ratios depending on the imaging depth observed with the dyes. (c) Fluorescence images obtained using different dyes at the selected depths of 25 μm (surface), 125 μm (mid-tissue), and 175 μm (deep-tissue). The boxed images are the magnified ones. The laser power was gradually increased from 5 mW to 95 mW (compensation excitation).
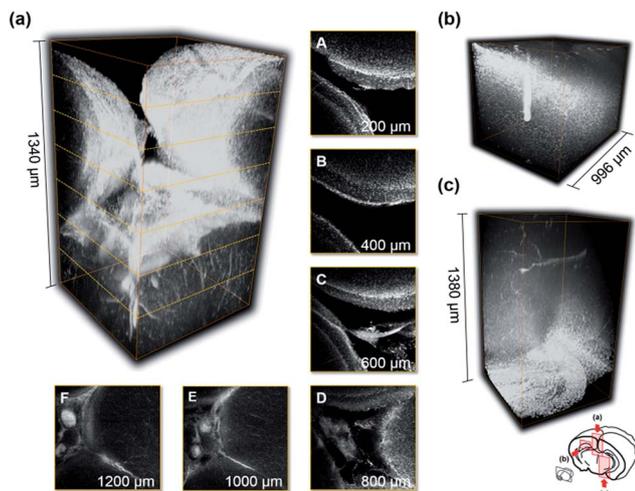
Fig. 5 Images from the (a) top, (b) side, and (c) bottom, which were collected through the red channel (625–675 nm) at every 2 μm of depth under excitation at 900 nm. (A–F) z-Direction cross-section images at different depths from the top. The laser power was gradually increased from 5 mW to 50 mW (compensation excitation). The field of view (FOV) was 775 μm × 775 μm.

Conclusions

Autofluorescence becomes a serious issue in the imaging of tissue by conventional laser scanning confocal microscopy, limiting its use to a shallow depth. Two-photon microscopy based on a two-photon absorbing dye allows for deep tissue imaging while maintaining a high resolution and thus has gained increasing importance in studying biological processes beyond the cellular level. We have conducted a systematic study to establish autofluorescence interference that is dependent on the type of tissue, excitation wavelength, and emission wavelength channels (of blue, green, yellow, and red) in two-photon imaging.

Among the five mouse organ tissues examined, brain, kidney, liver, lung, and spleen, the kidney tissue exhibited prominent autofluorescence followed by the liver, and others. Above all, regardless of the tissue type or excitation wavelength, much higher autofluorescence occurs not only from the green but also from the yellow emission channels where common two-photon absorbing dyes also emit, whereas minimal autofluorescence occurs from the red channel. Two-photon excitation at 900 nm resulted in lower autofluorescence than that observed under excitation at 850 nm or less, albeit the difference is small. In order to obtain deep tissue images with high resolution and to assess the imaging depth that is dependent on the dyes, we have developed a novel class of pyridinium-benzocoumarin dyes that emit in the far-red region and show high water solubility and high photostability. A comparison of the tissue images obtained with three different fluorophores that cover different emission channels (blue-green, yellow, and red) but have comparable two-photon action cross-sections reveals that the use of the far-red emitting dye is superior to others to image the deeper tissue region. The results provide

fundamental guidelines for deep tissue imaging using two-photon microscopy, and also inspires us to develop small molecular two-photon absorbing dyes that are bright and far-red or NIR emitting. Application of the far-red emitting dyes to develop fluorescent probes for disease biomarkers is anticipated.

Experimental

General information on materials

The chemical reagents were purchased from Sigma-Aldrich or Alfa-Aesar or TCI and used as received. All of the solvents were purified and dried by standard methods prior to use. Deionized water was used to prepare all aqueous solutions. ^{1}H and ^{13}C NMR spectra were recorded on a Bruker 300 MHz, 500 MHz or 600 MHz spectrometer using tetramethylsilane as the internal reference. All chemical shifts are reported in the standard notation of parts per million (ppm) using residual solvent protons as the internal standard. Infrared spectra were recorded on a Shimadzu IR-470 spectrometer. The melting points were determined using a thermogravimetric analyser (TGA, SII EXSTAR 6000) and a differential thermal analyser (DTA) at a heating rate of 10 °C per minute under a nitrogen environment. Mass spectroscopic data were obtained from the Korea Basic Science Institute (Daegu) using a JEOL JMS 700 high resolution mass spectrometer.

Fluorescence assays of the dyes

UV/vis absorption spectra were obtained using a HP 8453 UV/Vis spectrophotometer. Fluorescence spectra were recorded on a Photon Technology International fluorimeter with a 1 cm standard quartz cell. The excitation and emission wavelength band paths were both set at 2 nm. All of the solvents used were of analytical grade. The solution was allowed to cool down to room temperature before carrying out spectrometric measurements. A stock solution of each of the **Py⁺BC** dyes was prepared in dimethyl sulfoxide (DMSO) at a concentration of 10 mM. A required amount of the mixed solution was transferred to a cuvette (1.0 mL) for spectroscopic measurement. In the case of an aqueous solution, it was added to the aqueous solvent by keeping the concentration of DMSO within 1% of the total volume. The final titrant volume is the same for all measurements (1.0 mL).

Preparation of mice tissue samples and their TPM imaging

The experimental procedures regarding mice tissues herein were performed in accordance with protocols approved by The Pohang University of Science and Technology Committee on Animal Research and we followed the guidelines for the use of experimental animals established by The Korean Academy of Medical Science. We made every effort to minimize animal suffering and reduce the number of animals used to prepare samples for imaging. Balb/C type mice (6 weeks) were used for this experiment. Basically, the experiments were conducted under light protected conditions (in a dark-room and using aluminum foil). The mouse was dissected after dislocation of

the cervical vertebra. The five organs (brain, lung, liver, kidney and spleen) were removed and washed with PBS buffer. For the autofluorescence analysis, these samples were used without a staining step. For the experiments for the dye dependent imaging depth comparison, tissues were incubated in the PBS buffer solution containing 10 μM of each dye for 24 h in an incubator maintained with 5% of CO_2 in the air and at 37 °C. The stained sample was washed with PBS buffer three times to remove the remaining dye on the surface and then sliced with a vibrating blade microtome (VT1000S, Leica, Germany) in 50 μm thickness. Each of the sliced samples was placed on a slide glass for imaging, and images of the tissue sample were recorded using two-photon microscopy (2PM). 2PM imaging was performed using a Ti-Sapphire laser (Chameleon Vision II, Coherent) at a 140 fs pulse width and 80 MHz pulse repetition rate (TCS SP5 II, Leica, Germany) through a 20 × objective lens (obj. HCX PL APO 20×/1.10 W CORR CS, Leica, Germany). The two-photon excitation wavelength for the dye was tuned to 800, 850, and 900 nm. Each emission light was spectrally resolved into four channels ($\lambda_{em, blue}$ = 430–480 nm, $\lambda_{em, green}$ = 500–550 nm, $\lambda_{em, yellow}$ = 565–605 nm, $\lambda_{em, red}$ = 625–675 nm). The tissue samples were prepared as above and were mounted on a tight-fitting holder. The excitation laser power was applied in the compensation manner from 5 to 95 mW in all of the experiments. The images consist of 1024 × 1024 pixels, and the scanning speed was maintained at 200 MHz during the entire imaging process. The acquired images were processed using the software LAS AF Lite (Leica, Germany).

Signal-to-noise (S/N) ratio calculation

To calculate the signal-to-background ratio, all images were analyzed using Matlab 2013. The average signal and background intensities of each individual image from every 2 μm of depth were measured from three kidney samples stained with dyes that have different colors. The signal-to-background ratio (R) is defined as follows:

$$R = \left(\sum_{i \in \text{signal}} \frac{I_s^i / N_s}{\sum_{i \in \text{B.G}} I_b^i / N_b} \right)$$

Here, 'I' and 'N' are the fluorescence signal intensity in a region of interest (ROI) and the number of the pixels in the ROI in the "signal" or "background" region, respectively ('i' is maintained as 7 in the whole experiment).[35]

BABB clearing of the whole brain and its TPM imaging

According to the procedures described above, we prepared mouse tissue samples. The brain was removed from the skull and placed in fixative for 24 h at room temperature, rinsed 2 times in PBS, and stored in PBS containing 20 μM of **Py⁺BC690** for 24 h. After being washed with PBS 3 times, the stained brain was dehydrated in gradually increased methanol-buffer solutions (once in 50%, once in 80%, and twice in 100% methanol solutions for 3 min each) at room temperature. The whole brain tissue was rinsed with hexane to obtain maximal dehydration, and it was transferred into a clearing solution of 1 : 2 benzyl

alcohol (Sigma)/benzyl benzoate (Sigma). The brain tissue was stored in the clearing solution for 12 h at room temperature before imaging.[33] The whole brain tissue was placed on a slide glass, which was covered with a cover glass supported with a hand-made bracket. The brain images were recorded using 2PM. The two-photon excitation wavelength for the probe was tuned to 900 nm. The emission light was collected in the red channel (λ_{em} = 625–675 nm). The excitation laser power was applied in the compensation manner from 5 to 50 mW. The images consist of 512 × 512 pixels, the scanning speed was maintained at 400 MHz during the entire imaging process, and the images were collected in every 2 μm of depth. The acquired images were processed using LAS AF Lite (Leica, Germany), and the 3D tissue images were constructed using Matlab 2013.

Conflicts of interest

There are no conflicts to declare.

Acknowledgements

Notes and references

1 U. D. Monte, *Cell Cycle*, 2009, **8**, 505–506.
2 W. Denk, J. H. Strickers and W. W. Webb, *Science*, 1990, **248**, 73–76.
3 W. R. Zipfel, R. M. Williams and W. W. Webb, *Nat. Biotechnol.*, 2003, **21**, 1369–1377.
4 D. Kobat, N. G. Horton and C. Xu, *J. Biomed. Opt.*, 2011, **16**, 106014–106017.
5 D. Kleinfeld, P. P. Mitra, F. Helmchen and W. Denk, *Proc. Natl. Acad. Sci. U. S. A.*, 1998, **95**, 15741–15746.
6 K. Svoboda, F. Helmchen, W. Denk and D. W. Tank, *Nat. Neurosci.*, 1999, **2**, 65–73.
7 F. Helmchen, K. Svoboda, W. Denk and D. W. Tank, *Nat. Neurosci.*, 1999, **2**, 989–996.
8 Y. Imanishi, K. H. Lodowski and Y. Koutalos, *Biochemistry*, 2007, **46**, 9674–9684.
9 P. Theer, M. T. Hasan and W. Denk, *Opt. Lett.*, 2003, **28**, 1022–1024.
10 E. Kobat, M. E. Durst, N. Nishimura, A. W. Wong, C. B. Schaffer and C. Xu, *Opt. Express*, 2009, **17**, 13354–13364.
11 R. Kawakami, K. Sawada, A. Sato, T. Hibi, Y. Kozawa, S. Sato, H. Yokoyama and T. Nemoto, *Sci. Rep.*, 2013, **3**, 1014–1020.
12 M. Pawlicki, H. A. Collins, R. G. Denning and H. L. Anderson, *Angew. Chem., Int. Ed.*, 2009, **48**, 3244–3266.
13 M. M. M. Raposo, C. Herbivo, V. Hugues, G. Clermont, M. C. R. Castro, A. Comel and M. Blanchard-Desce, *Eur. J. Org. Chem.*, 2016, **2016**, 5263–5273.

14 L. Gu, D. J. Hall, Z. Qin, E. Anglin, J. Joo, D. J. Mooney, S. B. Howell and M. J. Sailor, *Nat. Commun.*, 2013, **4**, 2326–2332.

15 A. Purc, B. Koszarna, I. Iachina, D. H. Friese, M. Tasior, K. Sobczyk, T. Pedziński, J. Brewer and D. T. Gryko, *Org. Chem. Front.*, 2017, **4**, 724–736.

16 H. M. Kim and B. R. Cho, *Chem. Rev.*, 2015, **115**, 5014–5055.

17 W. R. Zipfel, R. M. Williams, R. Christie, A. Y. Nikitin, B. T. Hyman and W. W. Webb, *Proc. Natl. Acad. Sci. U. S. A.*, 2003, **100**, 7075–7080.

18 (*a*) A. R. Sarkar, C. H. Heo, H. W. Lee, K. H. Park, Y. H. Suh and H. M. Kim, *Anal. Chem.*, 2014, **86**, 5638–5641; (*b*) W. Sun, J. Fan, C. Hu, J. Cao, H. Zhang, X. Xiong, J. Wang, S. Cui, S. Sun and X. Peng, *Chem. Commun.*, 2013, **49**, 3890–3892; (*c*) L. Zhou, Q. Wang, Y. Tan, M. J. Lang, H. Sun and X. Liu, *Chem.–Eur. J.*, 2017, **23**, 8736–8740; (*d*) D. Frath, P. Didier, Y. Mély, J. Massue and G. Ulrich, *ChemPhotoChem*, 2017, **1**, 109–112; (*e*) Y. Ma, Y. Tang, Y. Zhao, S. Gao and W. Lin, *Anal. Chem.*, 2017, **89**, 9388–9393; (*f*) Z. Mao, W. Feng, Z. Li, L. Zeng, W. Lv and Z. Liu, *Chem. Sci.*, 2016, **7**, 5230–5235; (*g*) L. Guo, R. Zhang, Y. Sun, M. Tian, G. Zhang, R. Feng, X. Li, X. Yu and X. He, *Analyst*, 2016, **141**, 3228–3232.

19 S. Huang, A. A. Heikal and W. W. Webb, *Biophys. J.*, 2002, **82**, 2811–2825.

20 J. E. Aubin, *J. Histochem. Cytochem.*, 1979, **27**, 36–43.

21 N. J. Durr, C. T. Weissphenning, B. A. Holfeld and A. Ben-Yakar, *J. Biomed. Opt.*, 2011, **16**, 026008–026020.

22 R. Weissleder, *Nat. Biotechnol.*, 2001, **19**, 316–317.

23 D. Kim, H. Moon, S. H. Baik, S. Singha, Y. W. Jun, T. Wang, K. H. Kim, B. S. Park, J. Jung, I. Mook-Jung and K. H. Ahn, *J. Am. Chem. Soc.*, 2015, **137**, 6781–6789.

24 M. Tasior, D. Kim, S. Singha, M. Krzeszewski, K. H. Ahn and D. T. Gryko, *J. Mater. Chem. C*, 2015, **3**, 1421–1446.

25 H. Moon, Q. P. Xuan, D. Kim, Y. Kim, J. W. Park, C. H. Lee, H. J. Kim, A. Kawamata, S. Y. Park and K. H. Ahn, *Cryst. Growth Des.*, 2014, **14**, 6613–6619.

26 D. Kim, S. Singha, T. Wang, E. Seo, J. H. Lee, S. J. Lee, K. H. Kim and K. H. Ahn, *Chem. Commun.*, 2012, **48**, 10243–10245.

27 D. Kim, S. Sambasivan, H. Nam, K. H. Kim, J. Y. Kim, T. Joo, K. H. Lee, K. T. Kim and K. H. Ahn, *Chem. Commun.*, 2012, **48**, 6833–6835.

28 S. Nizamov, K. I. Willig, M. V. Sednev, V. N. Belov and S. W. Hell, *Chem.–Eur. J.*, 2012, **18**, 16339–16348.

29 S. Singha, D. Kim, B. Roy, S. Sambasivan, H. Moon, A. S. Rao, J. Y. Kim, T. Joo, J. W. Park, Y. M. Rhee, T. Wang, K. H. Kim, Y. H. Shin, J. Jung and K. H. Ahn, *Chem. Sci.*, 2015, **6**, 4335–4342.

30 J. B. Grimm, B. P. English, J. Chen, J. P. Slaughter, Z. Zhang, A. Revyakin, R. Patel, J. J. Macklin, D. Normanno, R. H. Singer, T. Lionnet and L. D. Lavis, *Nat. Methods*, 2015, **3**, 244–250.

31 K. Rurack and M. Spieles, *Anal. Chem.*, 2011, **83**, 1232–1242.

32 P. Hazra, D. Chakrabarty, A. Chakraborty and N. Sarkar, *Chem.Phys. Lett.*, 2004, **388**, 150–157.

33 P. Sarder, S. Yazdanfar, W. J. Akers, R. Tang, G. P. Sudlow, C. Egbulefu and S. Achilefu, *J. Biomed. Opt.*, 2013, **18**, 106012–106022.

34 H. U. Dodt, U. Leischner, A. Schierloh, N. Jährling, C. P. Mauch, K. Deininger, J. M. Deussing, M. Eder, W. Zieglgänsberger and K. Becker, *Nat. Methods*, 2007, **4**, 331–336.

35 R. Kawakami, K. Sawada, A. Sato, T. Hibi, Y. Kozawa, S. Sato, H. Yokohama and T. Nemoto, *Sci. Rep.*, 2013, **3**, 1014–1020.